RESEARCH ARTICLE

NANO · MICRO small
www.small-journal.com

Viologen-Derived Covalent Organic Frameworks: Advancing PFAS Removal Technology with High Adsorption Capacity

*Amin Zadehnazari, Ahmadreza Khosropour, Amin Zarei, Leila Khazdooz, Saeed Amirjalayer, Florian Auras, and Alireza Abbaspourrad**

The escalating presence of per- and polyfluoroalkyl substances (PFAS) in drinking water poses urgent public health concerns, necessitating effective removal. This study presents a groundbreaking approach, using viologen to synthesize covalent organic framework nanospheres: MELEM-COF and MEL-COF. Characterized by highly crystalline features, these nanospheres exhibit exceptional affinity for diverse anionic PFAS compounds, achieving simultaneous removal of multiple contaminants within 30 min. Investigating six anionic PFAS compounds, MEL- and MELEM-COFs achieved 90.0–99.0% removal efficiency. The integrated analysis unveils the synergistic contributions of COF morphology and functional properties to PFAS adsorption. Notably, MELEM-COF, with cationic surfaces, exploits electrostatic and dipole interactions, with a 2500 mg g^{-1} adsorption capacity—surpassing all reported COFs to date. MELEM-COF exhibits rapid exchange kinetics, reaching equilibrium within 30 min. These findings deepen the understanding of COF materials and promise avenues for refining COF-based adsorption strategies.

1. Introduction

Porous materials, such as covalent organic frameworks (COF), have emerged as powerful solutions for addressing water contamination issues, owing to their distinctive characteristics.[1] Formed through covalent bonds among organic molecules, COFs exhibit a crystalline network structure with a high specific surface area, regular repeating units, and exceptional chemical and thermal stability.[2,3] The versatility of COFs, with adjustable pore dimensions, positions them as highly effective tools for selectively adsorbing contaminants even within complex mixtures.[4] Strategic design, by incorporating specific building blocks and functional groups, enhances their interaction with targeted contaminants, making COFs potent adsorbents for the precision removal of selected substances. Beyond their impressive adsorption capacity, COFs offer additional advantages, including reusability and stability, making them appealing for pollutant mitigation.[5,6]

A particularly challenging class of contaminants is per- and polyfluoroalkyl substances (PFAS), these forever chemicals present substantial environmental and health threats.[7–9] Forever chemicals received this nickname because of their resistance to biological and chemical breakdown processes.[10] Their extensive usage and persistence have led to infiltration into various water sources. Adsorption is commonly used for PFAS removal, either as a standalone method or as part of a multi-stage treatment process incorporating steps like reverse osmosis or ion exchange.[11] Enhanced adsorption of PFAS entities can be strategically pursued through surface chemistry manipulation.[12] Specifically, the incorporation of functional groups that increase hydrogen bonding and electrostatic interactions within the material's framework increases the potential for selectively trapping and extracting PFAS species.[13,14] Another facet involves increasing surface area, which directly impacts the material adsorption capacity and facilitates enhanced adsorption efficiency.[15] Finally, precise control over the size and distribution of pores in porous materials has been found to influence PFAS adsorption dynamics.

Various solid adsorbents, including activated carbon,[16–18] anion-exchange resins,[19–21] porous organic polymers,[22,23] amino-functionalized sorbents, metal oxides,[24] and metal-organic frameworks (MOF),[25] have already been used for PFAS removal from contaminated water. The unique properties of COFs position them as a promising alternative for PFAS removal and retention.[26–29] While the use of COFs for PFAS removal is in its early stages, modification of the COF skeleton with diverse ionic building blocks or functional groups that capitalize on the COFs positively charged groups with the electronegative

A. Zadehnazari, A. Khosropour, A. Zarei, L. Khazdooz, A. Abbaspourrad
Department of Food Science
College of Agricultural and Life Sciences
Cornell University
Stocking Hall
Ithaca, NY 14853, USA
E-mail: Alireza@cornell.edu

S. Amirjalayer
Institute for Solid State Theory
Center for Nanotechnology and Center for Multiscale Theory and Computation
University of Münster
Wilhelm-Klemm-Straße 10, 48149 Münster, Germany

F. Auras
Faculty of Chemistry and Food Chemistry
TUD Dresden University of Technology
01217 Dresden, Germany

The ORCID identification number(s) for the author(s) of this article can be found under https://doi.org/10.1002/smll.202405176

DOI: 10.1002/smll.202405176

fluorine and oxygen atoms of the PFAS can significantly improve adsorption capacity.[30–32] In summary, COFs represent a frontier in PFAS removal.

Here, we report viologen-based COF materials, MELEM-COF and MEL-COF, for efficient PFAS removal from water. These COFs were fully characterized and used to study the underlying mechanisms of PFAS removal, comparing the performance of MELEM- and MEL-COF with conventional methods. Leveraging the unique COF properties of MELEM- and MEL-COF, this study reveals innovative approaches for contaminant elimination from water sources, aiming to enhance understanding and pave the way for cutting-edge water purification technologies.

2. Results and Discussion

2.1. Construction and Analysis of MELEM-COF and MEL-COF

Two COF materials were synthesized by a one-pot solvothermal synthesis involving the Zincke reaction of the Zincke salt (tetranitro viologen, TVN) with either of two triazine derivatives, heptazine and melamine, denoted as MELEM-COF and MEL-COF, respectively (**Scheme 1**)

The crystallinity of the materials was characterized by powder X-ray diffraction (PXRD). The PXRD patterns of the synthesized COF materials showed sharp and distinct peaks, indicating a highly crystalline structure. The major peaks observed at $2\theta = 3.96°$, 6.85°, 7.93°, 10.47°, and 26.61° for MELEM-COF are related to the (100), (2$\bar{1}$0), (200), (300), and (001) planes, respectively. Similarly, the peaks at $2\theta = 4.80°$, 8.31°, 9.63°, 12.63°, and 30.79° for MEL-COF can be assigned to the same crystallographic planes as those assigned for MELEM-COF (**Figure 1a,b**). The observed diffraction peaks were consistent with the expected hexagonal pore network of the COF material, indicating successful synthesis and crystallization. No additional diffraction peaks from impurities or other phases were observed, confirming the high purity of the synthesized COF material.

Simulated PXRD patterns were generated for the synthesized COF materials based on the crystal structure obtained from the PXRD analysis. The obtained simulated eclipsed (AA) and staggered (AB) patterns were compared with the experimental PXRD patterns. The positions and intensities of the major peaks in the simulated AA pattern matched well with the experimental patterns, confirming the hexagonal pore network of the COF material. Pawley refinement was performed to precisely refine the crystal structures MELEM-COF and MEL-COF to obtain accurate structural parameters and validate the PXRD peak assignments. The refinement results (Figure 1a,b, black curves) revealed well-ordered and regular hexagonal pore networks in both COFs, highlighting their high crystallinity and confirming the absence of significant deviations or structural disorder. For MELEM-COF, the unit cell parameters were determined to be $a = b = 25.6$ Å, $c = 3.46$ Å, with $\alpha = \beta = 90°$ and $\gamma = 120°$, in the space group $P3$. The refinement yielded satisfactory agreement with the experimental data, with $R_p = 5.0\%$ and $R_{wp} = 7.6\%$. The refined structure parameters exhibited excellent agreement with those obtained from simulation methods, indicating the absence of significant deviations or structural disorders. For the more crystalline MELEM-COF, we performed additional Rietveld refinement to investigate its structural details. The Rietveld refinement reinforced the high-quality crystallographic information, affirming the accuracy of the structural parameters obtained earlier through Pawley refinement. The Rietveld refinement resulted in $R_p = 22.9\%$ and $R_{wp} = 7.49\%$, which was in excellent agreement with the Pawley refinement data (see Supporting Information). Similarly, the Pawley refinement for MEL-COF yielded unit cell parameters of $a = b = 21.2$ Å, $c = 2.94$ Å, with $\alpha = \beta = 90°$ and $\gamma = 120°$, in the space group $P3$. The R_p and R_{wp} values were found to be 5.9% and 7.8%, respectively.

The chemical structure of the COFs was studied and compared with the monomers by FT-IR. The FT-IR spectra of the COF materials showed the characteristic vibration signals at 1600 and 840 cm^{-1} for the C═N and C—N bonds (Figure S1 and S2, Supporting Information). The disappearance of the amine (3280 and 3467 cm^{-1}) and nitro groups (1530 and 1339 cm^{-1}) in the spectrum of the COF materials indicated the successful conversion of the starting materials into the desired products.[33]

Solid-state cross-polarization magic angle spinning carbon-13 nuclear magnetic resonance (CP/MAS ^{13}C-NMR) spectra of COF material showed well-resolved signals, which is consistent with a highly ordered and crystalline structure (Figure S3 and S4, Supporting Information). The signals were assigned to different types of carbon atoms based on their chemical shifts and their coupling with neighboring nuclei. The most prominent signals in the spectra were observed in the range of 110–146 ppm, which correspond to the sp^2 hybridized carbon atoms in the aromatic rings of the COF. The presence of multiple signals in this region indicates the presence of different types of aromatic rings in the structure, which is consistent with the expected diversity of building blocks used in the synthesis of these COFs. In addition to the signals from the aromatic rings, a strong signal was also observed at about 159 ppm, which corresponds to the sp^2 hybridized carbon atom of the N—C═N bond in the triazine and linker units of the COF material.

The morphology of MELEM-COF and MEL-COF was examined using field-emission scanning electron microscopy (FE-SEM) and high-resolution transmission electron microscopy (HRTEM). FE-SEM images revealed spherical particles with a uniform distribution for both COFs, with average diameters of 129.9 ± 2.78 nm for MELEM-COF and 212.7 ± 2.20 nm for MEL-COF (Figure S5a, S6a, S7, and S8, Supporting Information). Energy dispersive X-ray spectroscopy (EDS) analysis confirmed the presence of carbon, nitrogen, oxygen, and chlorine in both COFs, indicating successful viologen unit incorporation (Figure S5b and S6b, Supporting Information). SEM-EDS mapping showed homogenous element distribution in MELEM-COF, with carbon backbone uniformity and nitrogen incorporation. Chloride acts as a counter ion for the positively charged nitrogen atoms of the viologen unit, its presence confirms the viologen units' integration.[34] While the oxygen detected was an impurity likely from environmental moisture, the carbon dioxide treatment or minor residual solvent trapped in the framework.[35]

HRTEM images exhibited nanospherical morphologies with lattice fringes, confirming a layered structure with pores. MELEM-COF displayed hexagonal channels within nanospheres, with a lattice spacing of 3.5 Å, indicating a highly crystalline structure (**Figure 2d–g**).[36] MEL-COF exhibited well-defined lattice fringes composed of eighteen layers, emphasizing the consistent interlayer distance of 2.6 Å, due to the robust crystalline

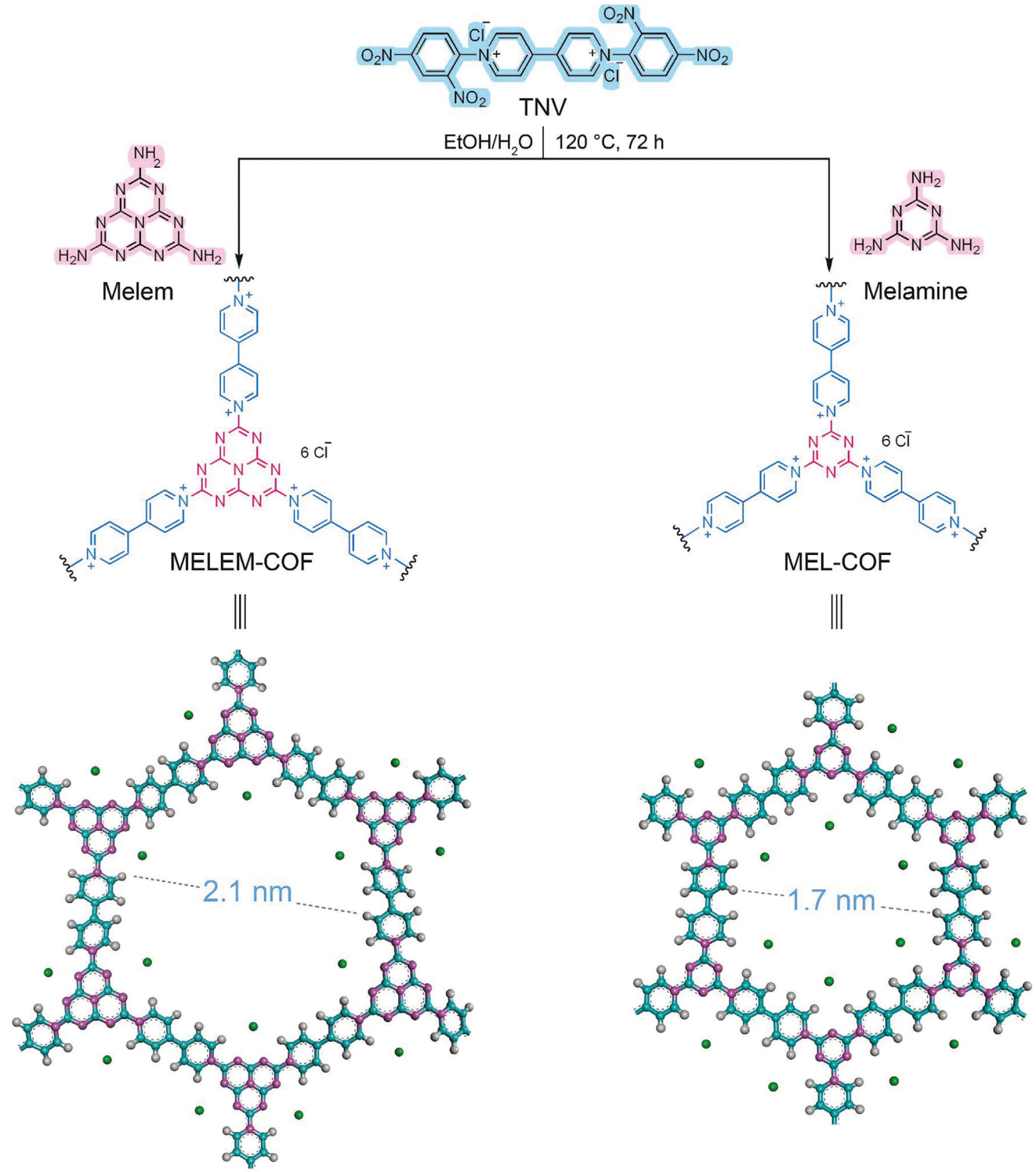

Scheme 1. Schematic scope for the synthesis of MELEM-COF and MEL-COF

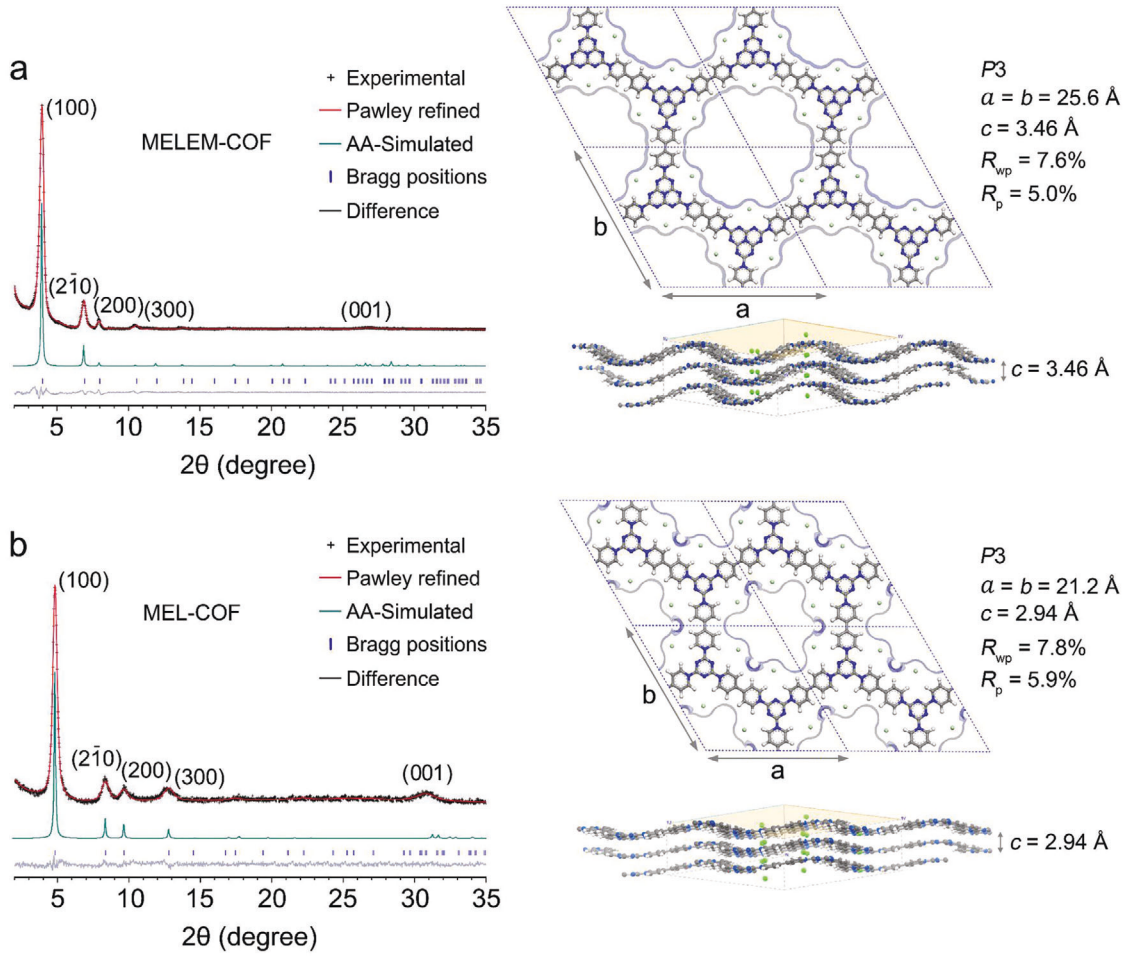

Figure 1. PXRD patterns for MELEM-COF (a) and MEL-COF (b). The experimental PXRD profiles (red) are compared with the refined Pawley patterns (depicted in black), alongside the simulated pattern corresponding to the AA stacking model (green), Bragg positions (blue), and a differential plot (shaded in gray) for a comprehensive comparison. Inset: Representation of the crystal unit cell of both MELEM-COF and MEL-COF. Diverse atom types are visually differentiated by color: C atoms in gray, H atoms in white, N atoms in blue, and Cl^- ions in green. Insets: Top and side views of COF unit cell with Connolly surfaces for an N_2-sized probe.

structure of the MEL-COF (Figure S10e, Supporting Information). The FFT patterns confirmed the highly crystalline structures with hexagonal facets (Figure 2d, bottom inset; Figure S10c, Supporting Information).[37] Selected area electron diffraction (SAED) patterns of MELEM-COF and MEL-COF indicated various crystal surfaces that align with diffraction peaks (Figure 2 g; Figure S10d, Supporting Information).

We performed N_2 adsorption-desorption experiments at 77 K to investigate the porosity and validate the stacking model of MELEM-COF and MEL-COF. In the isotherm plots (Figure 2i), both materials displayed a pronounced increase in the low-pressure range ($P/P_0 = 0 – 0.01$), suggesting a microporous nature in line with IUPAC classification.[38] The BET surface areas of MELEM-COF and MEL-COF, calculated within the range of $P/P_0 = 0.01 – 0.15$, were determined to be 1272 and 935 $m^2 g^{-1}$, respectively (Figure S12, Supporting Information). Additionally, we identified substantial pore volumes of 0.570 $cm^3 g^{-1}$ for MELEM-COF and 0.325 $cm^3 g^{-1}$ for MEL-COF. We analyzed the pore size distributions of MELEM-COF and MEL-COF using quenched solid density functional theory (QSDFT) and our experimentally found N_2 adsorption isotherm data at 77 K. By comparing the experimental adsorption isotherms with cylindrical equilibrium kernels, we determined that the average pore widths were 2.02 nm for MELEM-COF and 1.87 nm for MEL-COF (Figure S13, Supporting Information). These findings are consistent with the values derived from the simulated models of 2.1 and 1.7 nm (Scheme 1).

The viologen units in the COF backbone contributed to positive surface charges, as indicated by zeta potential values of +38.2 mV and +29.3 mV for MELEM-COF and MEL-COF (Figure S14, Supporting Information).

UV–vis diffuse reflectance spectroscopy (DRSUV) and steady-state fluorescence analysis were used to investigate the optical characteristics and band gaps of COFs (Figure S15a, Supporting Information). A semiconductor-like absorption in the blue region, indicative of semiconductor band structures, was observed for all samples. Density functional theory (DFT) revealed that the visible light response of COFs originates from electron

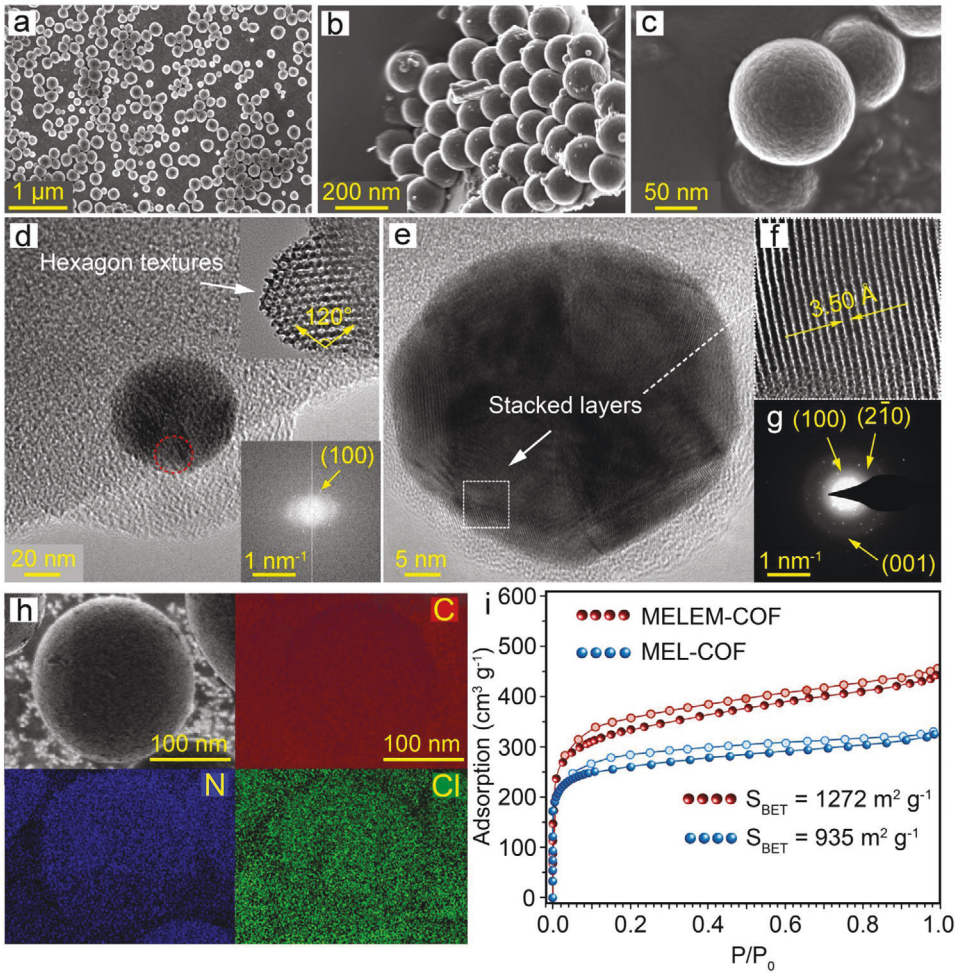

Figure 2. a–c) Field-emission scanning electron microscopy (FE-SEM) micrographs of spherical MELEM-COF particles. The average size of particles is 130 nm. d) High-resolution transmission electron microscopy (HRTEM) images showcasing a MELEM-COF particle, displaying uninterrupted lattice fringes spanning its entirety. The top inset presents the cross-sectional HRTEM image of the corresponding particle, indicating the presence of hexagonal apertures. The arrows represent a 120° angle between two adjacent sides. The bottom inset in (d) is the Fast Fourier Transform (FFT) of the highlighted region (enclosed in a red circle), cropped to emphasize the dominant fringe spacing and confirm the existence of diverse crystalline phases. e, f) Overview image of one MELEM-COF particle, serving as the basis for a more detailed image obtained from a specific area of interest (the marked white area). This close-up reveals multiple layers that are stacked. By zooming in on the layered segment, the interlayer distance and layer thickness become obvious. The profile shown in panel (f) illustrates a consistent and unbroken pattern, marked by an approximate periodicity of 3.5 Å. g) Selected area electron diffraction (SAED) pattern obtained from HRTEM. The arrows point to the diffraction rings associated with crystal unit cell planes. h) Energy-dispersive X-ray spectroscopy (EDS) mapping images of MELEM-COF. i) N_2 adsorption and desorption isotherms of MELEM-COF (red) and MEL-COF (blue).

transitions between the valence band (VB) populated by N 2*p* orbital to the conduction band (CB) formed by C 2*p* orbital.[39] Both MELEM-COF and MEL-COF exhibited photo-absorption ability from UV to visible light, with absorption edge wavelengths at ≈670 and 625 nm, respectively. The bathochromic shift in the maximum absorption edge value for MELEM-COF, attributed to its larger π-conjugated system,[40] results in optical semiconductor band gaps of 2.07 and 2.20 eV for MELEM-COF and MEL-COF respectively (Figure S15b, Supporting Information).[41]

Under 395 nm excitation, MEL-COF and MELEM-COF exhibited maximum emission peaks at 620 and 656 nm, respectively (Figure S15c, Supporting Information). The bathochromic shift in the emission peak of MELEM-COF indicated a lower energy transition state, attributed to its more extensive π-conjugated system.[42] This enhanced delocalization of π-electrons in MELEM-COF led to a longer excited-state lifetime (Figure S15d, Supporting Information), with a measured lifetime of 3.51 ns compared to 2.38 ns for MEL-COF. The extended excited-state lifetime of MELEM-COF is linked to its superior electronic structure, providing a greater number of possible electronic transitions and relaxation pathways.[43] These luminescent properties underscore the potential of MELEM-COF for applications requiring efficient electronic transitions and longer excited-state lifetimes.

DFT analysis of the COFs revealed HOMO-LUMO gaps of 1.87 eV for MELEM-COF and 2.05 eV for MEL-COF (Figure S15e and S16, Supporting Information), consistent with the observed optical bandgaps.[44,45] DFT simulations show that the electron distribution spans the entire molecule in both HOMO and LUMO levels. In the HOMO, electrons concentrate around

heptazine or melamine units, whereas LUMO states primarily exhibit amplitude around the viologen units, with little density on the positive nitrogen. Notably, the compounds exhibit their lowest energy absorption during the primary dipole-allowed π–π^* electronic transition. This transition highlights the intramolecular charge transfer processes as it shapes the optical properties of these materials.[46]

X-ray photoelectron spectroscopy (XPS) was used to investigate the chemical states of surface elements in COFs (Figure S17 and S18, Supporting Information). Despite the structural similarity of the two COFs, high-resolution spectra of Cl 2*p*, Cl 2*s*, C 1*s*, N 1*s*, and O 1*s* showed marked differences. MELEM-COF had weak peaks at 196.33 (± 0.021) and 267.17 (± 0.020) eV, corresponding to Cl 2*p* and Cl 2*s* XPS signals. The C 1*s* spectrum of MELEM-COF showed peaks at ≈284.40 (± 0.017) and 287.63 eV (± 0.015) which were assigned to C—C and C—N bonds, respectively. Similarly, the N 1*s* spectrum showed peaks at 398.32 (± 0.018) and 400.51 (± 0.023) eV, attributed to N—C in the heptazine system and N—C in BPy^{2+} moieties.[47] The intensity ratio of N—C in the heptazine ring to imine N—C in BPy^{2+} was ≈6:1 for MELEM-COF and 3:1 for MEL-COF, consistent with expectations. The peak observed ≈405.10 (±0.012) eV in the N 1s spectrum has been attributed to nitro groups.[48] Oxygen signals at 531.5 and 531.9 eV in both MELEM-COF and MEL-COF, potentially from defects or external sources like moisture, ethanol, atmospheric O_2, nitro end groups from viologen units or adsorbed CO_2 on the surface, may have implications for structural attributes.[35]

2.2. Chemical and Thermal Stability

The thermal stability of MELEM-COF and MEL-COF was analyzed using TGA/DTG under a nitrogen atmosphere (Figure S19, Supporting Information). Both COFs exhibited remarkable stability up to 480 °C, suitable for high-temperature applications. MELEM-COF showed a 5% weight loss at 524 °C, while MEL-COF had a slightly higher loss at 493 °C due to its higher aromatic content. Both displayed a single-step degradation process, indicating well-defined mechanisms and predictable thermal behavior.[49]

The chemical stability of MELEM-COF and MEL-COF was assessed under different conditions, revealing remarkable resilience. Both COFs maintained stability after exposure to boiling water, 3 M HCl, and 3 M NaOH for 72 h. FT-IR spectra exhibited minimal changes indicating preserved structural integrity (Figure S20 and S21, Supporting Information), although under acid treatment an expected peak at 3440 cm^{-1} was observed and attributed to the protonation of the nitrogens of the heptazine and triazine units.[50] PXRD patterns confirmed sustained high crystallinity after treatment (Figure S22 and S23, Supporting Information). Analysis of surface morphology, particle shape, and distribution quality showed no discernible alterations post-treatment (Figure S24 and S25, Supporting Information). Under basic conditions radical cations formed, indicated by a distinct signal in the electron paramagnetic resonance (EPR) spectra (Figure S26 and S27, Supporting Information).

The synthesized networks demonstrated unique interconnected architectures through the Zincke reaction, transmitting electric charge from the aromatic heptazine and triazine nucleus to the viologen component. Remarkably, re-oxidation of the reduced COFs to their original dicationic forms in the presence of acid showed no apparent structural degradation, exhibiting lower EPR signal intensities compared to the reduced forms obtained in the presence of base.[30]

The hydrophilicity of the COF surfaces was measured using contact angles. MELEM-COF showed a 52° angle, indicating higher hydrophilicity, while MEL-COF had a 68° angle, suggesting lower hydrophilicity (Figure S28 and S29, Supporting Information). Differences stem from porosity and surface charge variations in the cationic COFs. MELEM-COF's lower angle and higher hydrophilicity were linked to its higher porosity and increased positive charge. These properties will increase MELEM-COFs ability to interact with water.[51]

2.3. Adsorption of PFAS Substances

We measured the ability of MELEM- and MEL-COFs to absorb PFAS materials starting with perfluorooctanoic acid (PFOA) in Milli-Q (MQ) water. A 1 mg L^{-1} solution of PFOA was treated with a 100 mg L^{-1} suspension of the COFs, for 1 h at room temperature (≈25 (C). Solutions treated with MELEM-COF had a final concentration of PFOA of 0.003 mg L^{-1} or a 99.7% removal efficiency, while those treated with MEL-COF had a final concentration of 0.007 mg L^{-1} or a 99.3% removal efficiency (LC-MS detection limit for PFOA is 4.1 ng L^{-1}). Compared to reported removal efficiencies for similar COFs, both MELEM- and MEL-COF exhibited much higher removal efficacy of PFOA.[12] Additional investigations explored their adsorption capabilities, comparing kinetic behavior in PFOA adsorption over a 2 h period, and collecting data at 5 min intervals. Both COFs followed the linear pseudo-second-order kinetic model (Figure S30–S33, Supporting Information). The rate constant for PFOA adsorption using MELEM-COF was determined to be 1263 g mg^{-1} h^{-1}, while for MEL-COF, it was 419 g mg^{-1} h^{-1}. MELEM-COF showed exceptional PFOA removal, with a final concentration of 0.01 mg L^{-1} exceeding 99.0% removal efficiency within 30 min. Because of MELEM-COFs superior performance, we explored the possible hydrophobic and electrostatic interactions that have been reported as mechanisms governing PFAS adsorption onto solid adsorbents.[52–54]

Critical factors influencing PFAS adsorption by COFs include surface area, charge, pore size, shape, and particle size of the adsorbents. The positive surface charge in both COFs, attributed to quaternary ammonium groups, confirms electrostatic interactions as primary mechanisms for PFOA removal by MELEM-COF and MEL-COF.[55] Zeta potentials indicate that MELEM-COF, with a higher positive charge, offers more active sites for PFOA adsorption than MEL-COF. MELEM-COF's larger surface area (1272 m^2 g^{-1}) also contributes to enhanced performance, and despite a minimal difference in pore size (21 Å for MELEM-COF, 17 Å for MEL-COF), both factors are considered crucial for absorption. Finally, MELEM-COF's smaller particle size (130 nm) enhances dispersion in water, providing more accessible active sites for PFOA adsorption compared to MEL-COF (212 nm).

The unfunctionalized nitrogen atoms within each COF significantly influence PFOA adsorption. MELEM-COF has seven nitrogen atoms per ring, and we attribute this to its better

PFOA adsorption than MEL-COF which contains half as many nitrogens.[56] Evaluating binding sites, MELEM-COF displayed a PFOA adsorption isotherm that fit well to the Langmuir model, with experimental data showing excellent alignment and a regression value of 0.99 (Figure S34 and S35, Supporting Information). According to the Langmuir isotherm, the estimated maximum capacity (Q_m) was determined to be ≈2500 mg g^{-1}, which represents the highest capacity for PFOA adsorption among all porous polymers and COFs reported so far (Table S1, Supporting Information). The high affinity is further confirmed by a calculated affinity coefficient (K_L) of 66240 L mol^{-1}. In contrast, the Freundlich isotherm did not fit well with the experimental results (regression value of 0.73), emphasizing the superior suitability and accuracy of the Langmuir model for the proposed mechanism. MELEM-COF's Freundlich constant (K_F) was determined as 376.2 (mg g^{-1}) (L mg^{-1})$^{(1/n)}$, where *n* is 2.4. For MEL-COF, the PFOA adsorption isotherm indicates a Q_m of 2000 mg g^{-1} (Figure S38, Supporting Information).

The influence of pH on PFOA adsorption using MELEM-COF was investigated at pH 5, 7, and pH 9, for each experiment the concentrations of MELEM-COF and PFOA were 100 and 0.2 mg L^{-1}, respectively. The results showed high adsorption efficiency, reaching a final concentration of 0.001 mg L^{-1}, 99.5% removal at pH 5, 0.0008 mg L^{-1}, 99.6% removal at pH 7, and 0.0012 mg L^{-1}, 99.4% removal at pH 9 (Figure S40, Supporting Information). These findings indicate that variations in pH do not significantly affect the adsorption efficiency of MELEM-COF in the removal of PFOA from water.

The selectivity of MELEM-COF for PFOA removal was evaluated in the presence of various inorganic and organic substances routinely found in natural waters. Selectivity studies were conducted using common anions present in drinking water, including sulfate, carbonate, chloride, and nitrate, provided by NaCl, $NaNO_3$, Na_2SO_4, and K_2CO_3. The impact of alginic acid and tannic acid—representative of natural organic matter—on PFOA adsorption was also assessed. For each experimental setup, PFOA, individual pollutants, and MELEM-COF were introduced into MQ water, the initial concentration of PFOA was 0.2 mg L^{-1}, and each individual salt and acid concentration was 5 mg L^{-1}, the solution was then treated with a 100 mg L^{-1} suspension of the COFs. A control experiment was performed by adding the same amounts of PFOA and COF to MQ water without any additional organic or inorganic substances. The results indicated that MELEM-COF selectively adsorbed PFOA from the contaminated water, showing minimal interference from both inorganic and organic pollutants on the PFOA adsorption efficiency (**Figure 3a**).

To evaluate MELEM-COF's effectiveness in eliminating low concentrations of a diversity of PFASs, we used the following PFAS compounds: perfluorobutanoic acid (PFBA), perfluorohexanoic acid (PFHA), perfluorooctanoic acid (PFOA), perfluorodecanoic acid (PFDA), perfluorooctane sulfonic acid (PFOS), and perfluoro-2-methyl-3-oxahexanoic acid (GenX). These experiments were performed individually in MQ water over a 30 min timeframe with an initial concentration of each PFAS compound at 20 µg L^{-1} and MELEM-COF concentration of 100 mg L^{-1}. For PFAS compounds with longer carbon chains (GenX, PFOA, PFOS, and PFDA), the final concentration of these PFASs was 0.2 µg L^{-1} such that removal rates exceeded 99.0% (Figure 3b). (The LC-MS detection limits for each COF for our system are: GenX 2.4 ng L^{-1}; PFOS 1.6 ng L^{-1}; PFDA 2.2 ng L^{-1}; PFHA 1.4 ng L^{-1}; PFBA 8.4 ng L^{-1}). PFBA is notoriously difficult to remove due to its shorter chain and higher water solubility, previously reported COFs have only achieved removal efficiencies of PFBA ranging from 60.0% to 90.0%.[29,57,58] Remarkably, MELEM-COF demonstrated remarkably high efficiency for the removal of shorter-chain PFAS compounds, the final concentration of PFBA was 0.6 µg L^{-1} and for 0.2 µg L^{-1} for PFHA which corresponds to a 97.0% removal for PFBA and ≈99.0% for PFHA.[59] MELEM-COF's effectiveness in absorbing the more leachable, and more water-soluble short-chain anionic PFAS compounds from water is a substantial finding.

Building on the individual removal results and to assess MELEM-COFs possible selectivity of one PFAS over another, we prepared a mixture of PFBA, PFHA, GenX, PFOA, PFOS, and PFDA. The concentration of each PFAS was 20 µg L^{-1} for an overall concentration of the mixed PFAS of 1.2 mg $L^{-1.}$ A 20 mL aliquot of this mixture was then treated with a 100 mg L^{-1} suspension of MELEM-COF for 30 min. (Figure 3b). The longer chain PFAS, such as GenX, PFOA, PFOS, and PFDA, showed removal percentages exceeding 99.0% and final concentrations of each PFAS was close to 0.2 µg L^{-1}, while PFHA and PFBA showed slightly lower removal percentages of ≈98.0% removal with a final concentration of 0.4 µg L^{-1} and for PFHA a 93.0% removal with a final concentration of 1.4 µg L^{-1} (Figure 3b). These results strongly support MELEM-COF as one of the most efficient adsorbents for removing a wide array of anionic PFAS compounds from water.

Real-world concentrations of PFAS are relatively low with an average concentration of PFAS 1 µg L^{-1}.[60] Therefore, the performance of MELEM-COF for PFAS removal at real-world concentrations was investigated. A mixture containing PFBA, PFHA, GenX, PFOA, PFOS, and PFDA, along with MELEM-COF, was prepared in MQ water. Each PFAS was present at a concentration of 200 ng L^{-1}, and MELEM-COF was added at a concentration of 300 mg L^{-1}, with a total volume of 20 mL and an exposure time of 30 min. This mixture resulted in a total PFAS concentration of 1.2 µg L^{-1}, which is comparable to the average PFAS concentration found in contaminated groundwater sources.[61] In addition to the batch system, this experiment was also done using a continuous flow system (Figure S41 and movie S1, Supporting Information). The quantities of MELEM-COF and each PFAS were identical to those used in the batch system. Notably, in both the batch system and the continuous flow system, both PFOS and PFOA, the two most hazardous PFAS, were below the detection limits for our LC-MS. These concentration levels are also below the U.S. Environmental Protection Agency's advisory limit of 4 ng L^{-1} (Figure 3c).[62] Additionally, MELEM-COF removed PFBA, PFHA, and PFDA below instrumental detection limits in both batch and continuous systems which also underscores its exceptional performance. In the batch system, the final concentration of GenX was reduced to 3.6 ng L^{-1}, corresponding to a >98.0% removal rate; however, GenX was not detected in the continuous system.

To demonstrate the practical applications of MELEM-COF in removing PFAS from contaminated drinking water, competitive adsorption studies were conducted in both batch and continuous systems, similar to those performed in MQ water. A mixture of PFBA, PFHA, GenX, PFOA, PFOS, and PFDA was added to

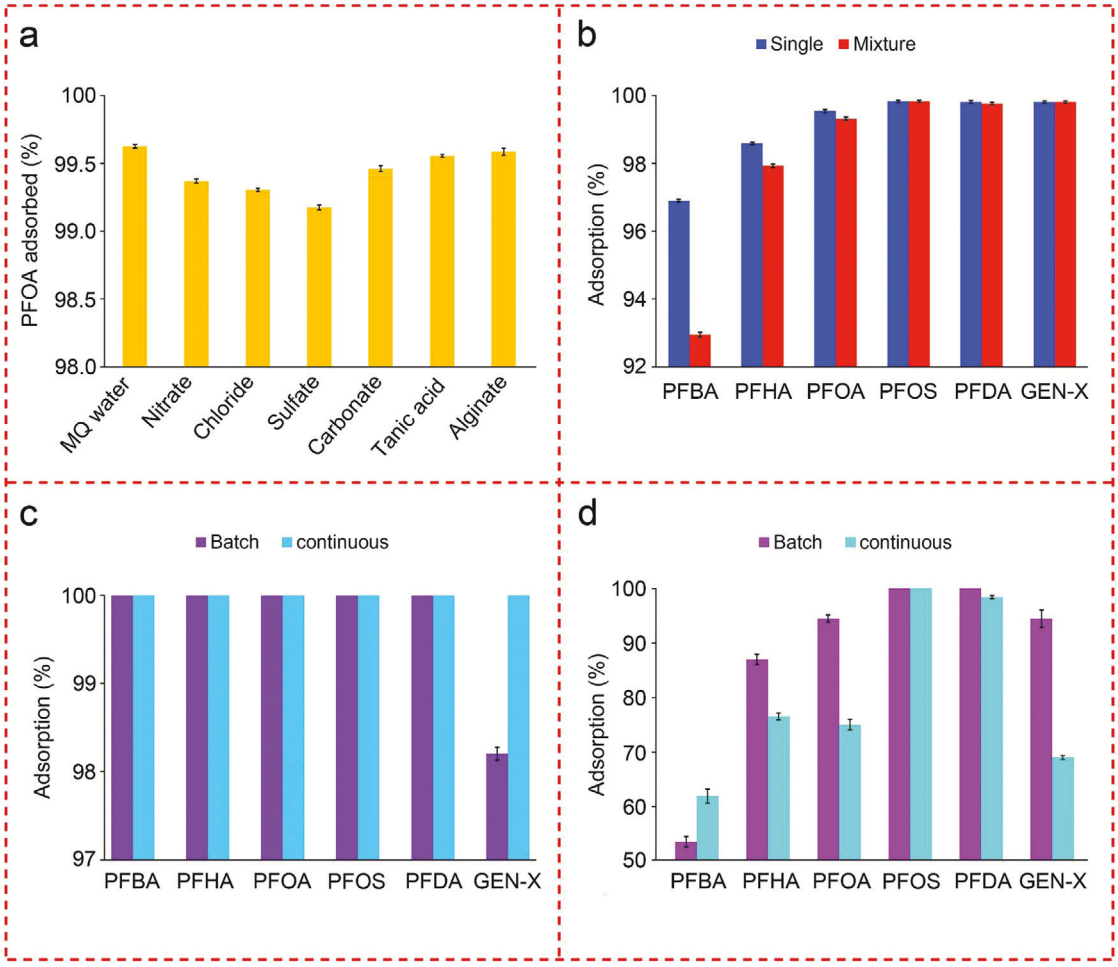

Figure 3. a) Effect of inorganic ions and natural organic matter (NOM) on the selective adsorption of PFOA by MELEM-COF after 30 min ($[PFOA]_0$ = 200 μg L^{-1}; [MELEM-COF] = 100 mg L^{-1}). b) Comparison of adsorption efficiency for six different PFAS by MELEM-COF in single-solute and multi-solute batch experiments after 30 min ($[PFOA]_0$ = 20 μg L^{-1}; [MELEM-COF] = 100 mg L^{-1}). c) Adsorption of various PFAS spiked in MQ water by MELEM-COF in multi-solute batch and continuous systems after 30 min (initial concentration of each PFAS was 200 ng L^{-1}; [MELEM-COF] = 300 mg L^{-1}). d) Competitive adsorption of various PFAS spiked in drinking water by MELEM-COF in multi-solute batch and continuous systems after 30 min (initial concentration of each PFAS was 200 ng L^{-1}; [MELEM-COF] = 300 mg L^{-1}). All measurements were conducted in triplicate. **Note**: Cases reported as 100.0% indicate that the concentrations were below the detection limits. The standard error bars are not represented in those cases.

Cornell University drinking water. As in the MQ water experiments, the concentration of each PFAS was set at 200 ng L^{-1}, while the MELEM-COF concentration was maintained at 300 mg L^{-1}. The exposure time was 30 min in both systems. Although dissolved components present in drinking water impacted the adsorbent, MELEM-COF still showed high-performance levels for the removal of PFAS from drinking water (Figure 3d). For example, PFOS was not detected in either system and in the continuous system, the concentration of PFOA decreased to 50 ng L^{-1}, while in the batch system, it decreased to 11 ng L^{-1}. Additionally, MELEM-COF exhibited almost complete removal of PFDA in both batch and continuous systems. For the less harmful PFAS compounds, PFBA, PFHA, and GenX, their concentrations were reduced to 93, 26, and 53 ng L^{-1} respectively in the batch system, and to 76, 47, and 62 ng L^{-1} in the continuous system.

The reusability of MELEM-COF was assessed through consecutive adsorption/desorption experiments. Following previously published regeneration procedures for other COFs using a methanol and NaCl solution mixture.[63,64] The quantity of PFOA adsorbed and desorbed during each cycle was quantified and showed sustained high efficiency (>99.0%) even after four cycles (Figure S42, Supporting Information).

PXRD analysis was done on the spent COF samples to assess the structural stability of MELEM-COF. The PXRD spectra of the MELEM-COF after PFAS adsorption showed intense and well-defined peaks, mirroring those of the as-synthesized COF (Figure S43, Supporting Information). The preservation of peak intensity indicates the retention of crystallinity even after multiple cycles of adsorption and desorption, suggesting robust structural stability under the applied conditions. FT-IR was used to examine any potential changes in the chemical structure of the COF during the adsorption-desorption cycles. Fortunately, no discernible alterations were observed in the FT-IR spectra of the spent MELEM-COF compared to the pristine material

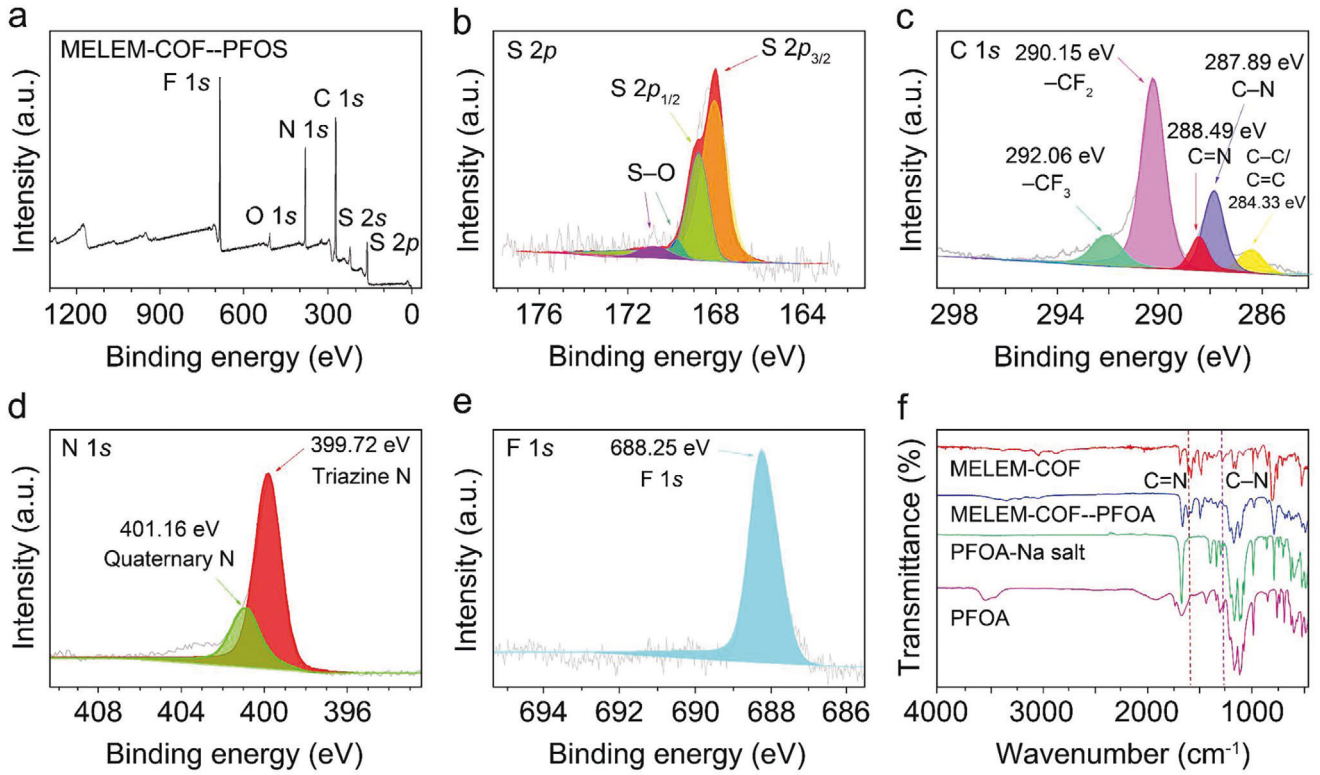

Figure 4. a) XPS spectra of PFOS-adsorbed MELEM-COF. XPS survey spectra along with the spectra of S 2*p* (b), C 1*s* (c), N 1*s* (d), and F 1*s* (e). f) Comparison of the FT-IR spectra of MELEM-COF before and after adsorption of PFOA: Neat MELEM-COF (red), PFOA-adsorbed MELEM-COF (blue), PFOA sodium salt (green), and pure PFOA (pink).

(Figure S44, Supporting Information). This consistency implies that the fundamental chemical structure of the COF remained unaltered throughout the successive adsorption and desorption processes.

2.4. Mechanistic Studies

The interactions between PFAS and MELEM-COF were investigated using PFOS and PFOA as representative compounds. Comparing the XPS spectra of MELEM-COF before and after PFOS sorption revealed distinct changes (**Figure** 4a–e). As expected, two new energy bands emerged in the F 1*s* and S 2*p* bands post-PFOS sorption, providing strong evidence of PFOS adsorption within the inner pores or on the surface of MELEM-COF. The absence of the Cl 2*p* signal in the XPS spectra of MELEM-COF following PFOS sorption indicates ion exchange.[65]

In the high-resolution XPS spectrum of S 2*p*, the S $2p_{3/2}$ and S $2p_{1/2}$ peaks were observed at ≈168.11 (± 0.017) and 168.92 eV (± 0.022), respectively, while the S—O peaks appeared at 169.86 (± 0.015) and 171.88 (± 0.018) eV. To quantitatively differentiate between different carbon bonding states in PFOS-adsorbed MELEM-COF, the C 1*s* peaks were fitted, considering an asymmetrical tail at higher energies. The fitting distinguished between five carbon bonding states: C—C/C=C (284.33 eV), C—N (287.89 eV), C=N (288.49 eV), CF_2 (290.15 eV), and CF_3 (292.06 eV).[66] Additionally, the XPS spectra displayed two contributions in the N 1*s* region, with one associated with lattice triazine nitrogen binding energy at 399.72 (± 0.020) eV and the other associated with quaternary nitrogen at 401.16 (± 0.015) eV.[66] Furthermore, a significant fluorine content was observed, with a corresponding binding energy of 688.25 (± 0.015) eV.

XPS analysis further confirmed PFOA adsorption on MELEM-COF. Similar to PFOS-adsorbed MELEM-COF, the disappearance of Cl 2*p* and Cl 2*s* peaks in the XPS spectrum of PFOA-adsorbed MELEM-COF (Figure S45, Supporting Information) indicated Cl^- ion replacement by PFOA, confirming the adsorption process. Distinct F 1*s* and N 1*s* peaks, along with a shift in the N 1*s* peak position, further confirmed successful PFOA adsorption. Additionally, EDS mapping was used to assess element distribution and concentration, with findings for PFOS-adsorbed MELEM-COF elements (Figure S46 and Table S2, Supporting Information).

In the FTIR, the vibrational peak shift at 1275 cm^{-1} in the C—N functional group of MELEM-COF becomes noticeable after PFOS adsorption, indicating an interaction between aromatic nitrogen groups electron donors) and quaternary nitrogen groups (electrostatically interacting with PFOS's ionic head) (Figure 4f).[67]

Density functional theory (DFT) was used to probe the interaction mechanisms facilitating the capture of PFAS by cationic COFs. Given the pKa values of PFOS and PFOA, which are −3.27 and 0.5 respectively, it is evident that these compounds exist in their deprotonated forms in water. DFT analysis showed that the bipyridine rings, situated in highly positive potential

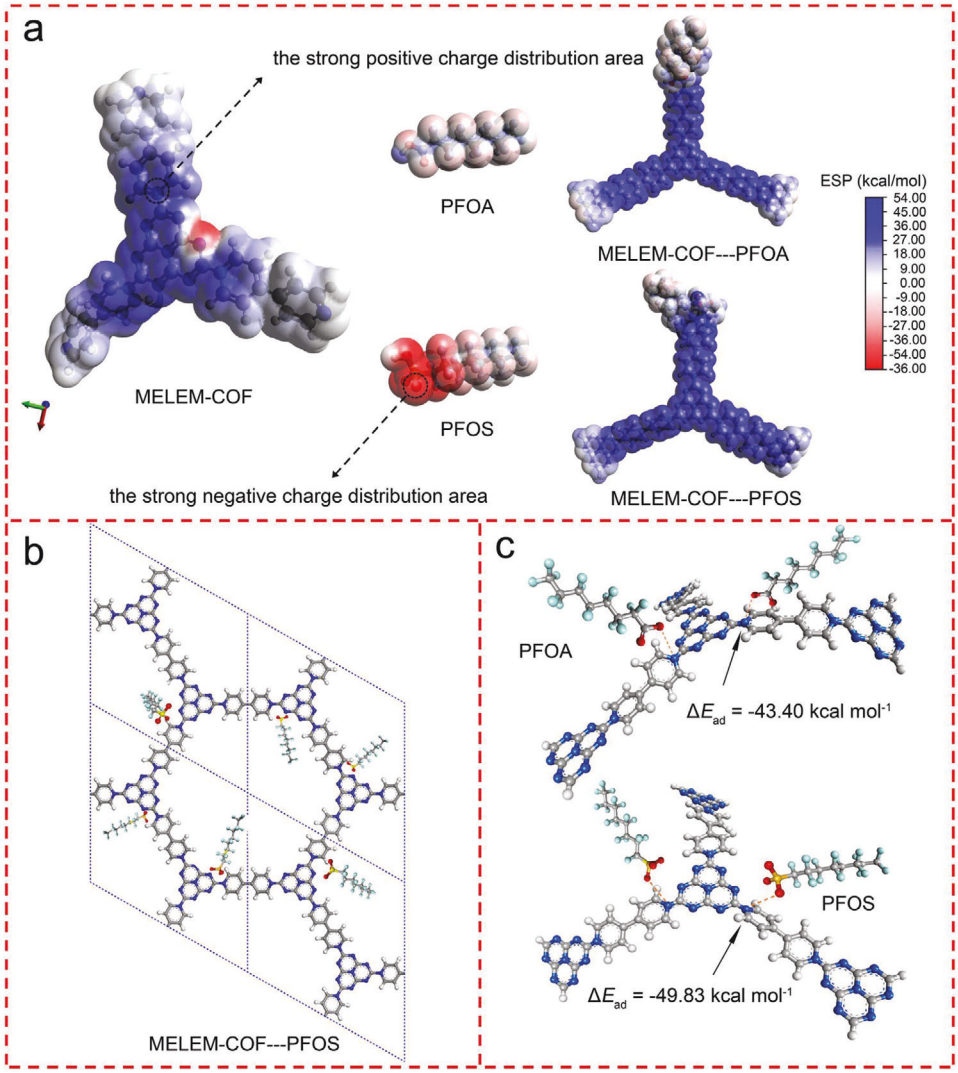

Figure 5. a) The Electrostatic surface potentials (ESP) are depicted with color gradients on the van der Waals surface ($\rho = 0.05$ a.u.) of each system. The color bar corresponds to the range of ESP values, providing a visual representation of the electrostatic characteristics of the individual components and their combined complex. b) Top view depicting perfluorooctane sulfonic acid (PFOS) on MELEM-COF. c) Visualization of the optimized geometry of a unit cell within MELEM-COF, demonstrating the interplay between diverse binding sites and PFOA as well as PFOS. The elements are color-coded (C in gray, N in blue, O in red, H in white, F in cyan), and electrostatic interactions, are denoted by yellow dash lines.

regions within the COF structures, serve as nucleophilic sites attracting the deprotonated carboxyl and sulfonyl groups of PFAS molecules such as PFOA and PFOS. This interaction is a key driver in the adsorption process, underscoring the role of specific electrostatic interactions between PFAS molecules and the COF (**Figure** 5a; Figure S47a, Supporting Information). The DFT calculations for anionic PFAS align with our experimental observations, offering further support for our findings. Specifically, the XPS analysis revealed a notable shift in the binding energy of quaternary nitrogen and the disappearance of the chlorine peak, underscoring anion exchange as the predominant mechanism in PFAS adsorption onto our synthesized ionic COFs. This theoretical and experimental concordance suggests a robust adsorption mechanism where PFAS molecules, once in solution, are initially drawn to the COF surfaces via electrostatic interactions with quaternary nitrogen elements. Subsequently, tighter adsorption occurs through ion exchange, anchoring PFAS molecules at the active sites.

Electrostatic surface potential (ESP) mapping on adsorbents helps to uncover adsorption behavior: Sites with high positive ESP are more likely to attract nucleophilic pollutants, such as PFASs, acting as active sites for their adsorption. Nucleophilic PFASs molecules were observed tightly adhering to the electrophilic regions of MELEM-COF or MEL-COF surfaces, demonstrating electrostatic complementation (Figure 5a; Figure S47a, Supporting Information). Notably, the oxygen end groups of PFAS exhibited highly negative ESP, while their C-F chain ends showed lower negative or even positive ESP, indicating that the oxygen-containing part is the primary site for COF adsorption.

When analyzing the ESP of COFs, it was observed that the quaternary nitrogen atoms of bipyridinium units are markedly

electropositive, whereas the nitrogen atoms within the heptazine and triazine frameworks exhibit a slightly negative charge.

MELEM-COF stands out with a higher ESP compared to MEL-COF, suggesting a stronger capacity for electrostatic interactions with PFAS molecules. This difference in ESP is critical for adsorption efficiency, as it directly influences the strength and specificity of the bond formed between the COF surfaces and PFAS. Essentially, the ESP of these materials dictates their interaction mechanism, as a higher positive potential enhances the material's ability to attract and bind with negatively charged pollutant molecules.

Understanding the molecular dimensions of PFAS is crucial for designing COFs with optimal pore sizes to enhance adsorption efficiency. Each COF unit (heptazine or triazine) in both MELEM-COF and MEL-COF includes three cationic bipyridinium units (Figure 5b; Figure S47b, and S48, Supporting Information). Using Gauss View software simulations, the molecular sizes of the PFAS molecules studied range between 4.9 to 9.8 Å (Figure S49, Supporting Information). The pore sizes of MELEM- and MEL-COF are roughly twice this size, thus ≈6 PFAS molecules can fit within each pore. Within the hexagonal COF structure, PFAS molecules can move into the pores, and anchor at the corners of the hexagonal shapes with the negative carboxylate or sulfonate groups oriented in close proximity to the positive pyridinium nitrogens. For both MELEM- and MEL-COF, the optimized average distances between the oppositely charged functional groups indicate the presence of electrostatic interactions in the cases of PFOA and PFOS.

The corresponding total adsorption energies (E_{ad}) were calculated, with values of −43.40 kcal mol^{-1} for PFOA and −49.83 kcal mol^{-1} for PFOS in MELEM-COF, and −35.91 kcal mol^{-1} for PFOA and −40.58 kcal mol^{-1} for PFOS in MEL-COF. The electrostatic interactions in COF–PFOA are relatively weaker than those in COF–PFOS.[68] Consequently, E_{ad} of COF–PFOA experiences a slight decrease to −43.40 kcal mol^{-1} for MELEM-COF and −35.91 kcal mol^{-1} for MEL-COF. In contrast, the E_{ad} values for PFOS adsorbed on these COFs remain higher at −49.83 kcal mol^{-1} for MELEM-COF and −40.58 kcal mol^{-1} for MEL-COF.

To delve deeper into the variations in adsorption among two PFAS, PFOA and PFOS, on bubble surfaces, we acquired radial distribution function (RDF) curves for water molecules and the two PFAS (Figure S50, Supporting Information). These curves, illustrated by the g(r) values, the radius of gyration, defining the probability of finding water molecules at a specific distance from PFAS particles, had a pronounced peak at ≈1.8 Å. This distinctive peak signifies the establishment of stable hydrogen bonds between the carboxyl or sulfonic group of PFAS and water molecules within the simulation system.[69,70] Moreover, the contact angle measurements provided quantitative evidence of the increased hydrophobicity, revealing a notable shift in the wettability of the COF surface (Figure S51, Supporting Information). The contact angle of MELEM-COF was initially 52°. Following the adsorption of PFOA and PFOS, the contact angles changed to 64° and 70°, respectively. This observed increase in contact angle is directly associated with the hydrophobic nature of PFAS molecules. The observed enhancement in hydrophobicity has implications for the overall performance of COFs in adsorption processes, as it influences the affinity and efficiency of the material in capturing hydrophobic contaminants. This insight underscores the dynamic nature of COF surfaces and their responsiveness to the specific adsorbates present in the environment.

In the framework of NCI isosurfaces, the presence of red areas signifies areas of repulsive non-bonding overlap. Conversely, the blue and green areas are indicative of electrostatic interactions and weak van der Waals forces, respectively (**Figure 6a**; S52, Supporting Information).[71] Figure 6a indicates the electrostatic and hydrogen bonding interactions between MELEM-COF and PFOA, highlighting the strong electrostatic attractions and the weaker van der Waals interactions. Additionally, the electron density (ρ) and the Laplacian of electron density ($\Delta^2\rho$) at bond critical points (BCPs) were calculated (Figure 6b). For hydrogen bonding and weak interactions like van der Waals, ρ and $\Delta^2\rho$ typically ranged from −0.015 to −0.025 a.u. and from 0.0075 to 0.0125 a.u., respectively. The blue regions can be attributed to the electrostatic attraction between the bipyridinium nitrogens and the anionic heads of PFOA. The observed electrostatic repulsion is likely due to the interaction between the anionic head of PFOA (carboxylate group) and the nitrogen of heptazine. A strong hydrogen bonding interaction and an electrostatic attraction at −0.025 a.u. coexist with a weaker repulsive interaction at 0.025 a.u., indicating overall attractive interactions (Figure 6a). Spikes of negative density values signify stabilized interactions, further confirming the presence of electrostatic interactions (Figure 6b; Figure S53, Supporting Information). The spikes with negative density values due to the polar head of PFOA and the positive nitrogen-containing bipyridinium units were more pronounced than other sites. This observation suggests that both MELEM-COF and MEL-COF possess a heightened capacity for forming robust electrostatic interactions with PFOA.

Unlike traditional ion-exchange resins and other nitrogen-containing materials, MELEM-COF and MEL-COF feature a unique spatial arrangement of nitrogen heteroatoms and quaternary nitrogen sites. This architecture facilitates not only specific electrostatic interactions but also optimizes van der Waals interactions across the COF structure. The generated contour maps reveal a distinct, symmetrically distributed negative van der Waals potential region, characterized by an ellipsoidal shape that enhances the attraction toward polar bonds in PFAS molecules. This specific interaction geometry is a direct consequence of the deliberate design and synthesis of our COFs, aimed at maximizing adsorption efficiency through both electrostatic and van der Waals forces.

The electron density provides a clear distinction between interactions, indicated by the peak at sign(λ_2)ρ(r) ≈ −0.05, and other intermolecular interactions represented by a broad band around zero density. The 3D plot facilitates the identification of bonding regions corresponding to each of these peaks. Hydrogen bonds and electrostatic interactions manifest as localized, circular, and blue NCI domains, specifically in the region where nitrogen and hydrogen atoms interact. Additionally, a complementary incipient peak with sign(λ_2)ρ(r) ≈ 0.05 appears as a red rim surrounding the electrostatic and hydrogen bond domains. A color-filled map with contour lines was generated to show the van der Waals potential in MELEM-COF complexes interacting with PFOA. This approach illustrates the van der Waals interactions between the chemical system and the external environment, exemplified by a carbon atom probe placed at a defined distance.[72,73] The van der Waals potential map specifically

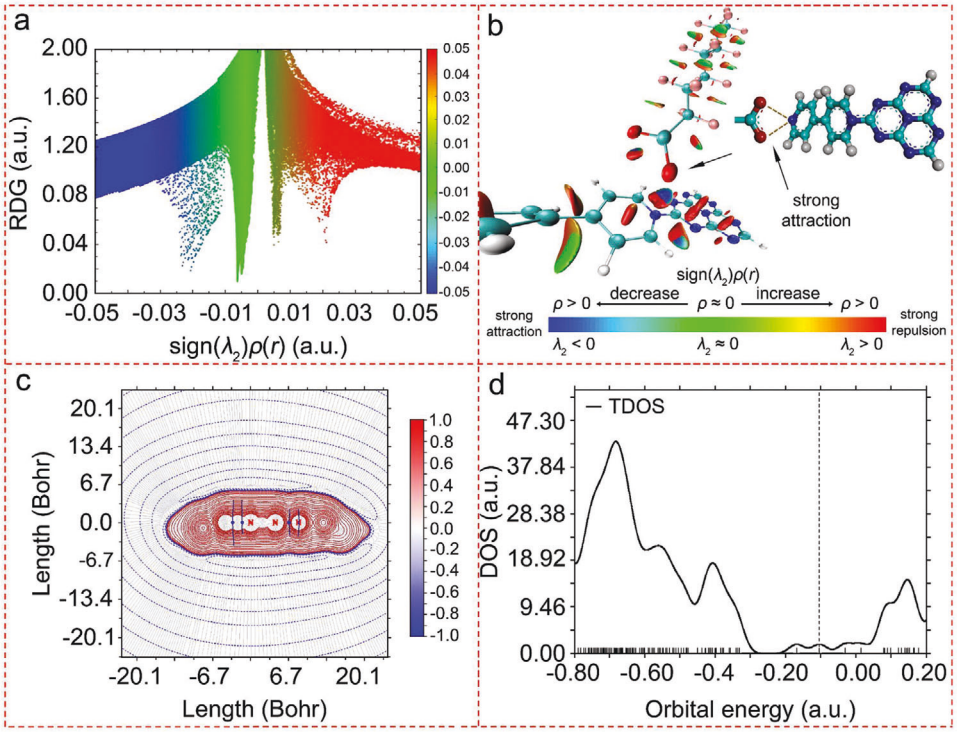

Figure 6. a) Non-covalent interaction map of the MELEM-COF—PFOA complex, emphasizing the region near zero corresponding to the crystal's electron density global minimum. b) NCI analysis for MELEM-COF—PFOA with isosurfaces colored to represent sign$(\lambda_2)\rho(r)$ values, ranging from −0.05 to 0.05 a.u. Blue indicates strong attractive interactions, green represents van der Waals interactions, and red signifies repulsive/steric interactions. c) Gradient line map of van der Waals potential of the MELEM-COF—-PFOA complex, showing interbasin paths and contour line corresponding to van der Waals surface ($\rho = 0.001$). The red-colored regions signify areas primarily influenced by exchange-repulsion potential, while the blue-colored regions denote those predominantly governed by dispersion-attraction potential. The color scale is given in kcal/mol. d) Density-of-states graph. The vertical dash line corresponds to the HOMO level at -0.1034 a.u. The height of the spikes reflects orbital degeneracy on the right axis.

represents the interaction energy between the current COF system and a probe atom of carbon placed at a defined distance, chosen due to the prevalence of carbon. The results were visualized in contour line maps (Figure 6c: Figure S54, Supporting Information) highlighting the chemically relevant negative region of the van der Waals potential. The positive isosurface was intentionally omitted for clarity. The maps illustrate that the region near nuclei is governed by exchange-repulsion potential, resulting in a substantially positive van der Waals potential. The negative portion exhibits a symmetric distribution resembling an ellipsoidal shape, making the entire area around the COF and PFOA susceptible to attraction due to bond polarity. The negative portion exhibits a symmetric distribution resembling an ellipsoidal shape, making the entire area around the COF and PFOA susceptible to attraction due to bond polarity. These findings emphasize robust interactions between exposed carbon and nitrogen sites in COF structures and PFAS polar bonds, contributing to outstanding adsorption performance.

The density-of-states (DOS) is a useful parameter for describing the motion states of electrons within materials, mapping the electronic landscape of a material, and providing details about the electronic structure and properties of materials, including their optical and electronic behaviors. The occupancy of these states, and the shape of the DOS bands, informs us about the probability of electron transitions, including transitions to the valence band, which are governed by Pauli's exclusion principle.[74] By examining the DOS maps, we learn how the electronic properties of materials are modified upon interaction with adsorbates. The total density-of-states (TDOS) plots corresponding to the pure MELEM-COF or MEL-COF, along with their interactions with PFOA were generated (Figure 6d; Figure S55–S57, Supporting Information). A comparison of the TDOS maps showed the electronic structure alterations induced by PFOA adsorption. This comparison identified the specific electronic interactions that facilitate the adsorption process.

Differences in TDOS maps such as shifts in energy levels and modifications in band shapes, suggest that the interaction between PFOA and the COF is not merely physical but involves substantial electronic reconfigurations, resulting from hybrid orbital interactions in the electronic shell of the system.[75] The analysis of the energy gap (ΔE) between the HOMO and LUMO across each system shows the potential for changes in optical transitions, which are pronounced in states involving different molecules.

The DOS analysis confirms the occurrence of an interaction between the COF and the PFAS entities and provides mechanistic insight. By examining how the electronic states of the COF are altered upon PFAS adsorption, the potential electronic interactions and changes in electron density distribution that facilitate the adsorption process can be inferred. Examination of the peak

heights reveals that all MOs within the COF-PFOA complexes lack degeneracy due to the molecular structure's low symmetry (Figure 6d; Figure S55–S57, Supporting Informations). In contrast, the free COFs exhibit numerous highly degenerate MOs owing to their elevated geometrical symmetry (D_{3h} point group). Consequently, these findings suggest a substantial alteration in the molecular electronic structure upon the formation of COF–PFOA complexes, underscoring the significant impact of PFOA on the orbital properties of the COFs.

3. Conclusion

In summary, the successful synthesis and characterization of highly crystalline viologen-based COFs, MELEM-COF and MEL-COF, which exhibited exceptional adsorption capabilities toward various PFAS compounds are presented. In practical terms, MELEM-COF proved highly effective in reducing the concentration of PFOA from 200 ng L^{-1} to less than 4.0 ng L^{-1}, surpassing the U.S. Environmental Protection Agency (EPA) advisory level. Additionally, MELEM-COF exhibited excellent regenerability, allowing for multiple cycles of reuse through simple methanol washing at ambient temperature. The remarkable performance observed in terms of adsorption capacity, selectivity, and kinetics is attributed to the cationic surfaces of these COFs, enabling electrostatic and dipole interactions with PFAS molecules, as confirmed by experimental and theoretical calculations. These findings not only contribute to our fundamental understanding of COF-based adsorption processes but also hold significant promise for the development of advanced water purification technologies targeting PFAS removal.

Supporting Information

Supporting Information is available from the Wiley Online Library or from the author.

Acknowledgements

The Cornell Center for Materials Research (CCMR) provided support for this project, courtesy of funding from the National Science Foundation under grant DMR-1719875. The authors also extend their gratitude for the utilization of the NMR facility at Cornell University, supported by the NSF through MRI grant number CHE-1531632. F.A. acknowledges funding from the Deutsche Forschungsgemeinschaft (DFG, German Research Foundation) – project No. 525243720.

Conflict of Interest

The authors declare no conflict of interest.

Data Availability Statement

The data that support the findings of this study are available from the corresponding author upon reasonable request.

Keywords

adsorption mechanism, covalent organic framework, microporous materials, PFAS

Received: June 25, 2024
Revised: July 21, 2024
Published online:

[1] K. Koner, S. Karak, S. Kandambeth, S. Karak, N. Thomas, L. Leanza, C. Perego, L. Pesce, R. Capelli, M. Moun, *Nat. Chem.* **2022**, *14*, 507.
[2] Y. Zhang, J. Guo, G. Han, Y. Bai, Q. Ge, J. Ma, C. H. Lau, L. Shao, *Sci. Adv.* **2021**, *7*, eabe8706.
[3] C. S. Diercks, O. M. Yaghi, *Science* **2017**, *355*, eaal1585.
[4] C. Kang, Z. Zhang, S. Kusaka, K. Negita, A. K. Usadi, D. C. Calabro, L. S. Baugh, Y. Wang, X. Zou, Z. Huang, *Nat. Mater.* **2023**, *22*, 636.
[5] A. Mellah, S. P. S. Fernandes, R. Rodríguez, J. Otero, J. Paz, J. Cruces, D. D. Medina, H. Djamila, B. Espiña, L. M. Salonen, *Chem. – Eur. J.* **2018**, *24*, 10601.
[6] C. Li, P. Guggenberger, S. W. Han, W.-L. Ding, F. Kleitz, *Angew. Chem., Int. Ed.* **2022**, *61*, 202206564.
[7] M. G. Evich, M. J. Davis, J. P. McCord, B. Acrey, J. A. Awkerman, D. R. Knappe, A. B. Lindstrom, T. F. Speth, C. Tebes-Stevens, M. J. Strynar, *Science* **2022**, *375*, eabg9065.
[8] B. Trang, Y. Li, X.-S. Xue, M. Ateia, K. N. Houk, W. R. Dichtel, *Science* **2022**, *377*, 839.
[9] B. Jin, H. Liu, S. Che, J. Gao, Y. Yu, J. Liu, Y. Men, *Nat. Water* **2023**, *1*, 451.
[10] C. Zhang, K. Yan, C. Fu, H. Peng, C. J. Hawker, A. K. Whittaker, *Chem. Rev.* **2021**, *122*, 167.
[11] T. Ruan, P. Li, H. Wang, T. Li, G. Jiang, *Chem. Rev.* **2023**, *123*, 10584.
[12] X. Liu, C. Zhu, J. Yin, J. Li, Z. Zhang, J. Li, F. Shui, Z. You, Z. Shi, B. Li, X.-H. Bu, A. Nafady, S. Ma, *Nat. Commun.* **2022**, *13*, 2132.
[13] K. R. Taibl, A. L. Dunlop, D. B. Barr, Y.-Y. Li, S. M. Eick, K. Kannan, P. B. Ryan, M. Schroder, B. Rushing, T. Fennell, *Nat. Commun.* **2023**, *14*, 3120.
[14] X. Tan, M. Sawczyk, Y. Chang, Y. Wang, A. Usman, C. Fu, P. Král, H. Peng, C. Zhang, A. K. Whittaker, *Macromolecules* **2022**, *55*, 1077.
[15] J. Lee, C. Kim, C. Liu, M. S. Wong, N. L. Cápiro, K. D. Pennell, J. D. Fortner, *Npj Clean Water* **2023**, *6*, 62.
[16] Y. Zhang, A. Thomas, O. Apul, A. K. Venkatesan, *J. Hazard. Mater.* **2023**, *460*, 132378.
[17] P. S. Pauletto, T. J. Bandosz, *J. Hazard. Mater.* **2022**, *425*, 127810.
[18] P. McCleaf, S. Englund, A. Östlund, K. Lindegren, K. Wiberg, L. Ahrens, *Water Res.* **2017**, *120*, 77.
[19] A. Maimaiti, S. Deng, P. Meng, W. Wang, B. Wang, J. Huang, Y. Wang, G. Yu, *Chem. Eng. J.* **2018**, *348*, 494.
[20] W. Wang, X. Mi, Z. Zhou, S. Zhou, C. Li, X. Hu, D. Qi, S. Deng, *J. Colloid Interface Sci.* **2019**, *557*, 655.
[21] Z. Du, S. Deng, Y. Chen, B. Wang, J. Huang, Y. Wang, G. Yu, *J. Hazard. Mater.* **2015**, *286*, 136.
[22] C. Ching, Y. Ling, B. Trang, M. Klemes, L. Xiao, A. Yang, G. Barin, W. R. Dichtel, D. E. Helbling, *Water Res.* **2022**, *209*, 117938.
[23] X. Liu, C. Zhu, J. Yin, J. Li, Z. Zhang, J. Li, F. Shui, Z. You, Z. Shi, B. Li, X.-H. Bu, A. Nafady, S. Ma, *Nat. Commun.* **2022**, *13*, 2132.
[24] M. Ateia, A. Alsbaiee, T. Karanfil, W. Dichtel, *Environ. Sci. Technol. Lett.* **2019**, *6*, 688.
[25] R. Li, S. Alomari, T. Islamoglu, O. K. Farha, S. Fernando, S. M. Thagard, T. M. Holsen, M. Wriedt, *Environ. Sci. Technol.* **2021**, *55*, 15162.
[26] L. Xiao, Y. Ling, A. Alsbaiee, C. Li, D. E. Helbling, W. R. Dichtel, *J. Am. Chem. Soc.* **2017**, *139*, 7689.
[27] W. Ji, L. Xiao, Y. Ling, C. Ching, M. Matsumoto, R. P. Bisbey, D. E. Helbling, W. R. Dichtel, *J. Am. Chem. Soc.* **2018**, *140*, 12677.
[28] J. Huang, Y. Shi, J. Xu, J. Zheng, F. Zhu, X. Liu, G. Ouyang, *Adv. Funct. Mater.* **2022**, *32*, 2203171.

[29] J. Huang, Y. Shi, G. Huang, S. Huang, J. Zheng, J. Xu, F. Zhu, G. Ouyang, *Angew. Chem., Int. Ed.* **2022**, *61*, 202206749.
[30] G. Das, T. Skorjanc, S. K. Sharma, T. Prakasam, C. Platas-Iglesias, D. S. Han, J. Raya, J.-C. Olsen, R. Jagannathan, A. Trabolsi, *ChemNanoMat.* **2018**, *4*, 61.
[31] C.-R. Zhang, W.-R. Cui, S.-M. Yi, C.-P. Niu, R.-P. Liang, J.-X. Qi, X.-J. Chen, W. Jiang, X. Liu, Q.-X. Luo, *Nat. Commun.* **2022**, *13*, 7621.
[32] F. Yu, J.-H. Ciou, S. Chen, W. C. Poh, J. Chen, J. Chen, K. Haruethai, J. Lv, D. Gao, P. S. Lee, *Nat. Commun.* **2022**, *13*, 390.
[33] R. Guo, Z. Zha, J. Wang, Z. Wang, M. D. Guiver, S. Zhao, *Small* **2023**, *20*, 2308904.
[34] W. He, S. Chandra, T. Quast, S. Varhade, S. Dieckhöfer, J. R. Junqueira, H. Gao, S. Seisel, W. Schuhmann, *Adv. Mater.* **2023**, *35*, 2303050.
[35] S. Zhang, G. Cheng, L. Guo, N. Wang, B. Tan, S. Jin, *Angew. Chem., Int. Ed.* **2020**, *59*, 6007.
[36] K. Cheng, H. Li, J.-R. Wang, P.-Z. Li, Y. Zhao, *Small* **2023**, *19*, 2301998.
[37] H. Heo, J. H. Sung, G. Jin, J.-H. Ahn, K. Kim, M.-J. Lee, S. Cha, H. Choi, M.-H. Jo, *Adv. Mater.* **2015**, *27*, 3803.
[38] M. Thommes, K. Kaneko, A. V. Neimark, J. P. Olivier, F. Rodriguez-Reinoso, J. Rouquerol, K. S. Sing, *Pure Appl. Chem.* **2015**, *87*, 1051.
[39] V. V. Shnitov, M. K. Rabchinskii, M. Brzhezinskaya, D. Y. Stolyarova, S. V. Pavlov, M. V. Baidakova, A. V. Shvidchenko, V. A. Kislenko, S. A. Kislenko, P. N. Brunkov, *Small* **2021**, *17*, 2104316.
[40] R. Berger, A. Giannakopoulos, P. Ravat, M. Wagner, D. Beljonne, X. Feng, K. Müllen, *Angew. Chem., Int. Ed.* **2014**, *53*, 10520.
[41] P. Kubelka, *Z. Tech. Phys.* **1931**, *12*, 593.
[42] K. Takagi, S. Yamamoto, K. Tsukamoto, Y. Hirano, M. Hara, S. Nagano, Y. Ie, D. Takeuchi, *Chem. – Eur. J.* **2018**, *24*, 14137.
[43] J. Zhang, M. Zhang, R.-Q. Sun, X. Wang, *Angew. Chem.* **2012**, *124*, 10292.
[44] J. Sworakowski, *Synth. Met.* **2018**, *235*, 125.
[45] D. Chen, H. Wang, *J. Phys. Chem. C* **2019**, *123*, 27785.
[46] K. Li, W.-D. Zhang, *Small* **2018**, *14*, 1703599.
[47] Z.-P. Dong, J.-J. Zhao, P.-Y. Liu, Z.-L. Liu, Y.-Q. Wang, *New J. Chem.* **2019**, *43*, 9032.
[48] Y. Chen, Z. Li, R. Ding, T. Liu, H. Zhao, X. Zhang, *J. Hazard. Mater.* **2022**, *426*, 128073.
[49] M. Jourshabani, M. R. Asrami, B.-K. Lee, *Small* **2023**, *19*, 2300147.
[50] G. Han, T. Hu, Y. Yi, *Adv. Mater.* **2020**, *32*, 2000975.
[51] R. S. Kingsbury, K. Bruning, S. Zhu, S. Flotron, C. T. Miller, O. Coronell, *Ind. Eng. Chem. Res.* **2019**, *58*, 18663.
[52] E. Gagliano, M. Sgroi, P. P. Falciglia, F. G. Vagliasindi, P. Roccaro, *Water Res.* **2020**, *171*, 115381.
[53] Y. Liu, T. Li, J. Bao, X. Hu, X. Zhao, L. Shao, C. Li, M. Lu, *Appl. Sci.* **2022**, *12*, 1941.
[54] M. Ateia, A. Alsbaiee, T. Karanfil, W. Dichtel, *Environ. Sci. Technol. Lett.* **2019**, *6*, 688.
[55] A. Mal, S. Vijayakumar, R. K. Mishra, J. Jacob, R. S. Pillai, B. S. Dileep Kumar, A. Ajayaghosh, *Angew. Chem.* **2020**, *132*, 8791.
[56] L. Chen, J. Song, *Adv. Funct. Mater.* **2017**, *27*, 1702695.
[57] A. Maimaiti, S. Deng, P. Meng, W. Wang, B. Wang, J. Huang, Y. Wang, G. Yu, *Chem. Eng. J.* **2018**, *348*, 494.
[58] A. Zaggia, L. Conte, L. Falletti, M. Fant, A. Chiorboli, *Water Res.* **2016**, *91*, 137.
[59] J. Li, X. Li, Y. Da, J. Yu, B. Long, P. Zhang, C. Bakker, B. A. McCarl, J. S. Yuan, S. Y. Dai, *Nat. Commun.* **2022**, *13*, 4368.
[60] J. Huang, Y. Shi, J. Xu, J. Zheng, F. Zhu, X. Liu, G. Ouyang, *Adv. Funct. Mater.* **2022**, *32*, 2203171.
[61] D. Mussabek, A. Söderman, T. Imura, K. M. Persson, K. Nakagawa, L. Ahrens, R. Berndtsson, *Water* **2023**, *15*, 137.
[62] K. Li, J. Hu, Q. Gu, J. He, Y.-K. Peng, Z. Xu, *ACS Appl. Mater. Interfaces* **2023**, *15*, 35107.
[63] X. Liu, C. Zhu, J. Yin, J. Li, Z. Zhang, J. Li, F. Shui, Z. You, Z. Shi, B. Li, *Nat. Commun.* **2022**, *13*, 2132.
[64] W. Wang, Z. Zhou, H. Shao, S. Zhou, G. Yu, S. Deng, *Chem. Eng. J.* **2021**, *412*, 127509.
[65] S. Mantripragada, S. O. Obare, L. Zhang, *Acc. Chem. Res.* **2023**, *56*, 1271.
[66] H. Yu, P. Zhang, H. Chen, Y. Yao, L. Zhao, M. Zhao, L. Zhu, H. Sun, *J. Hazard. Mater.* **2023**, 132748.
[67] W. Wang, Z. Zhou, H. Shao, S. Zhou, G. Yu, S. Deng, *Chem. Eng. J.* **2021**, *412*, 127509.
[68] J. Hao, Q. Zhang, P. Chen, X. Zheng, Y. Wu, D. Ma, D. Wei, H. Liu, G. Liu, W. Lv, *Environ. Sci. Nano* **2019**, *6*, 3374.
[69] A. Vishnyakov, A. V. Neimark, *J. Phys. Chem. B* **2001**, *105*, 7830.
[70] A. P. Lyubartsev, A. Laaksonen, *Phys. Rev. E* **1995**, *52*, 3730.
[71] J. Zhang, T. Lu, *Phys. Chem. Chem. Phys.* **2021**, *23*, 20323.
[72] T. Lu, F. Chen, *J. Mol. Graph. Model.* **2012**, *38*, 314.
[73] Z. Liu, T. Lu, Q. Chen, *Carbon* **2021**, *171*, 514.
[74] D. S. El-Sayed, *J. Mol. Model.* **2023**, *29*, 96.
[75] Z. Liu, T. Lu, Q. Chen, *Carbon* **2020**, *165*, 461.

